First Data from DM-Ice17

J. Cherwinka[a], D. Grant[b], F. Halzen[c], K. M. Heeger[c,f], L. Hsu[d], A. J. F. Hubbard[c], A. Karle[c], M. Kauer[c], V. A. Kudryavtsev[e], R. H. Maruyama[c,f,*], C. MacDonald[e], S. Paling[h], W. C. Pettus[c], Z. P. Pierpoint[c], B. N. Reilly[c], M. Robinson[e], P. Sandstrom[c], N. J. C. Spooner[e], S. Telfer[e], L. Yang[g]

(The DM–Ice Collaboration)

[a]*Physical Sciences Laboratory, University of Wisconsin, Stoughton WI, USA*
[b]*Department of Physics, University of Alberta, Edmonton, Alberta, Canada*
[c]*Department of Physics and Wisconsin IceCube Particle Astrophysics Center, University of Wisconsin-Madison, Madison, WI, USA*
[d]*Fermi National Accelerator Laboratory, Batavia, IL, USA*
[e]*Department of Physics and Astronomy, University of Sheffield, Sheffield, UK*
[f]*Department of Physics, Yale University, New Haven, CT, USA*
[g]*Department of Physics, University of Illinois at Urbana-Champaign, Urbana, IL, USA*
[h]*STFC Boulby Underground Science Facility, Boulby mine, Cleveland, TS13 4UZ, UK*

Abstract

We report the first analysis of background data from DM-Ice17, a direct-detection dark matter experiment consisting of 17 kg of NaI(Tl) target material. It was successfully deployed 2457 m deep in South Pole glacial ice at the bottom of two IceCube strings in December 2010 and is the first such detector to be operating in the Southern Hemisphere. Data from the first two years of operation after commissioning, July 2011 – June 2013, are presented here. The background rate in the 6.5 – 8.0 $\mathrm{keV_{ee}}$ region is measured to be 7.9 ± 0.4 counts/day/keV/kg. This is in agreement with the expected background from the crystal assemblies and is consistent with simulation. Background contributions from the surrounding ice were demonstrated to be negligible. The successful deployment and operation of DM-Ice17 establishes the South Pole ice as a location for future underground, low-background experiments in the Southern Hemisphere. The detector assembly, deployment, and analysis of the DM-Ice17 backgrounds are described.

Keywords: dark matter, direct detection, annual modulation, DAMA, South Pole, DM-Ice,

1. Introduction

Astrophysical and cosmological observations suggest that roughly 23 % of the Universe is cold dark matter [1]. Although evidence for dark matter has been firmly established [2, 3], its composition and characteristics remain largely unknown. Weakly Interacting Massive Particles (WIMPs) are theoretically favored because they can be produced in the early universe with the correct abundance to result in the observed relic density [4]. A suite of direct detection experiments is now underway to search for WIMPs through observation of WIMP-nucleon scattering [5–7].

We report on the performance of DM-Ice17, a NaI(Tl) direct dark matter detector deployed at the South Pole in December 2010. DM-Ice17 is designed to demonstrate the feasibility of operating a remote low-background NaI experiment to directly test the annual modulation of the WIMP-nucleon scattering rate observed by DAMA. The expected annual modulation arises from the motion of the Earth around the Sun and the motion of the Solar system through the dark matter halo of our galaxy [8, 9]. The DAMA/NaI [10] and DAMA/LIBRA [11] experiments, running at the Laboratori Nazionali del Gran Sasso for a combined 14 year period, have measured a consistent annual modulation at $9.3\,\sigma$, which they attribute to dark matter. More recently the CoGeNT [12, 13], CRESST [14], and CDMS-II(Si) [15] experiments have observed events in excess of the known backgrounds in their respective detectors. Under the assumption of elastic scattering of WIMPs, these results are inconsistent with exclusion limits set by several direct detection experiments

*Corresponding author
Email address: reina.maruyama@yale.edu (R. H. Maruyama)

for both spin-independent [16–21] and spin-dependent scattering cases [21–24].

New dark matter candidates [25–28], instrumentation effects [29], and modifications on the distributions of the local dark matter halo [30] have all been proposed in an attempt to reconcile these seemingly contradictory results with limited success.

A large radio-pure array of NaI(Tl) crystals placed deep in the Antarctic ice near the South Pole will have the ability to directly test DAMA's claim to have observed the annual modulation effect from dark matter in NaI(Tl) detectors [31]. The expected dark matter modulation would have a constant phase everywhere on Earth, whereas any modulation resulting from seasonal effects will reverse its phase between the Northern and Southern Hemispheres. The South Pole offers up to 2800 m of ice overburden, is extremely radio-pure, and strongly suppresses the effects of environmental and seasonal variations such as temperature, humidity, and pressure. Furthermore, the Amundson-Scott South Pole Station and IceCube Neutrino Detector offer technical infrastructure and muon veto capabilities [32].

2. Experimental Setup

2.1. Detector

DM-Ice17 consists of two 8.47 kg NaI(Tl) scintillating crystals in the South Pole ice, with each crystal coupled to two light guides and two photomultiplier tubes (see Fig. 1). Each detector assembly (denoted Det-1 and Det-2), along with its data acquisition and control electronics (see Sec. 2.2), is housed in its own stainless steel pressure vessel as a protection from the surrounding water and ice during deployment and operation. They are located at the bottom of two strings of IceCube [32] and are physically separated by 500 m (see Fig. 3).The NaI(Tl) crystals, light guides, and photomultiplier tubes (PMTs) are those used by the former NaIAD experiment which ran from 2000 – 2003 at the Boulby Underground Laboratory [33, 34]. They were stored in sealed copper boxes at the Boulby Underground Laboratory from 2003 – 2010, when they were retrieved to be used in DM-Ice17.

The two NaI(Tl) crystals, DM80 (Det-1) and DM81 (Det-2) in NaIAD publications, were produced by Bicron and re-encapsulated by Saint-Gobain. Previously measured background rates at 6 – 7 keV_{ee} of 7 – 10 counts/day/keV/kg are consistent with those observed in DM-Ice17 (see Sec. 5). These crystals provide well characterized detectors for this experiment, however the high background levels limit the sensitivity of DM-Ice17.

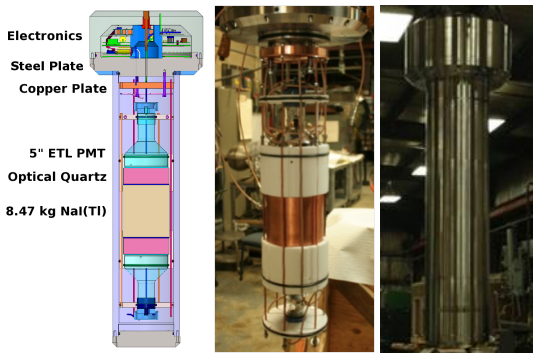

Figure 1: Engineering drawing (left) and photographs of one of the DM-Ice17 detectors with (right) and without (center) the stainless steel pressure vessel. The wider upper section of the stainless steel vessel contains the digitizing and control electronics, high voltage generation board, and isolation transformer for each PMT. The lower section houses one crystal (light brown in left fig) coupled to two PMTs (light blue) via quartz light guides (pink). Power and communication to the detector is provided through a "special devices" breakout from the main IceCube communication cable. The connection to the detector is made through a single penetrator at the top of the pressure vessel.

Each crystal measures 14.0 cm in diameter and 15.0 cm in length. For diffusive light reflection, the crystals are wrapped in thin sheets of PTFE (polytetrafluoroethylene). They are encapsulated with an oxygen-free high thermal conductivity (OFHC) copper housing and a thin quartz window on either end to protect the hygroscopic crystal. The encapsulation has an outer diameter of 14.6 cm and length of 16.5 cm.

The scintillation light is recorded by 5 inch 9390-UKB PMTs with C636-KFP voltage divider bases (Electron Tubes Limited). The 5 cm thick quartz light guides help shield the crystals from the radioactivity in the PMTs. A ~3 mm layer of Q900 silicone gel (Quantum Silicones) was used for optical coupling between the interfaces of the PMTs, light guides, and NaI(Tl) crystals. The gel also provided mechanical shock suppression between components during shipping and deployment. Q900, used in IceCube to couple the PMTs to the pressure housings, has been demonstrated to be robust, clean, and stable for long-term operation at the South Pole.

PTFE tubes (Applied Plastics Technology) serve to reflect light and provide mechanical support against lateral movements of the crystal, light guides, and PMTs. A PTFE disk around the base of each PMT maintains the alignment while Viton O-rings on the PTFE tubes and disks hold the detector centered in the pressure vessel. The optical components are tensioned together and further protected from mechanical shocks by six

threaded rods made of OFHC copper and a series of springs and nuts.

The detector assembly is suspended from a copper plate (orange in Fig. 1 left) which in turn hangs from a stainless steel mid-plate (gray in Fig. 1 left) separating the electronics from the lower volume. Holes for the wires were drilled at 45° through the steel plate to avoid direct line-of-sight to the optical components and potted with silicone-based epoxy. The lower pressure vessel volume was flushed with dry nitrogen and sealed from the electronics. The upper pressure vessel volume houses the electronics boards discussed in Sec. 2.2. A column of stainless steel (dark blue in Fig. 1) supports the electronics and adds mechanical strength to the wider top of the pressure vessel by transferring some of the load onto the mid-plate.

The stainless steel vessel protects the detectors from the pressure of the water column above and pressure spikes during freeze-in. The vessel is designed to withstand 10000 psi of external pressure. Pressure spikes exceeding 7000 psi have been observed by IceCube in deployment of previous strings. SANMAC SAF 2205 stainless steel tube stock (Sandvik) was used for the main body of the pressure vessel. The vendor was chosen as it is known to produce clean stainless steel, and the alloy was chosen for its mechanical properties (yield strength 0.2% = 450 MPa, tensile strength = 680 MPa). The seals were modeled after those used in IceCube's drill head and were tested to 7000 psi in a pressurized water chamber at UW-PSL.

Low background counting was performed at SNOLAB [35], with results summarized in Tab. 1. This counting included drill water, silicone gel, and excess stock from copper, stainless steel, and PTFE. It was not possible to screen materials prior to assembly due to the severe time constraints imposed by IceCube's deployment schedule; therefore, detector components and materials were selected from vendors known to produce radio-clean products. All machined components (*e.g.* pressure vessel, copper rods, screws) were cleaned using UHV cleaning techniques. The optical components were thoroughly cleaned with methanol and deionized water prior to assembly. The assembly of detector components was performed in the semi-clean room that was used for the IceCube modules.

2.2. Electronics and DAQ

Each PMT is independently controlled and monitored by its own IceCube Digital Optical Module Mainboard (DOM-MB) assembly and high voltage (HV) board [36] located in the top portion of the pressure vessel (see Fig. 2). The DOM-MBs are controlled remotely through a hub located in the IceCube Laboratory (ICL) on the surface of the ice. The hubs are remotely accessible via TCP/IP when there is a satellite connection to the South Pole Station or by the on-site personnel at any time.

The signal from each PMT is carried on an RG303 cable to the respective DOM-MB. The signal cables have the same length to provide identical signal transit times. The DOM-MBs contain a Field Programmable Gate Array (FPGA) that is configured with a simple version of IceCube's DAQ called "testDAQ" [36]. Analog PMT signals passing the trigger conditions are digitized by the DOM-MBs in four separate channels and sent to the hub at the ICL. The hub is synchronized to a GPS clock at the ICL and translates the DOM-MB timestamp into universal time, correcting for the cable lengths of 2500 m and 2995 m for Det-1 and Det-2 respectively.

The four digitization channels allow for different time windows and a broad dynamic range. The Flash Analog to Digital Converter (FADC) channel collects up to 256 samples at 40 MHz over a 6.4 μs window. The FADC channel has a gain of $\times$23.4 and 10-bit dynamic range. The three Analog Transient Waveform Digitizer (ATWD) channels each collect up to 128 samples at a programmable sampling rate of 100 – 500 MHz. Each ATWD channel has a 10-bit dynamic range but different gain: "ATWD0" at $\times$ 16, "ATWD1" at $\times$ 2, and "ATWD2" at $\times$ 0.25. Together the ATWD channels offer an effective dynamic range of 14-bits, allowing waveforms to be recorded without saturation from single photoelectrons (sub- keV) up to $>$ 20 MeV.

Although programmable, the run settings were held constant for all physics data presented here. The PMT HV settings were {1000, 1000, 1100, 950} V for {PMT-1a, PMT-1b, PMT-2a, PMT-2b}. PMT-1a and PMT-1b are the upper and lower PMTs coupled to Det-1 respectively (likewise for PMT-2a and PMT-2b in Det-2). The trigger threshold of each PMT was set to ~0.25 photoelectrons. A coincidence window of 800 ns was required to record the waveforms of the two PMTs coupled to the same crystal. The sampling rate of the DOM-Ice17 ATWD chips was set at ~200 MHz for a digitized waveform time window of ~640 ns. A ~1 ms deadtime is introduced during waveform digitization.

The DAQ records hardware monitoring information including temperature and pressure (measured at the DOM-MB) as well as PMT high voltage and trigger rate. Monitoring information, collected regularly during data taking, was recorded every 2 sec until February 2012 and every 60 sec since. The monitored parameters are discussed in Sec. 3 and the associated noise is discussed in Sec. 6.

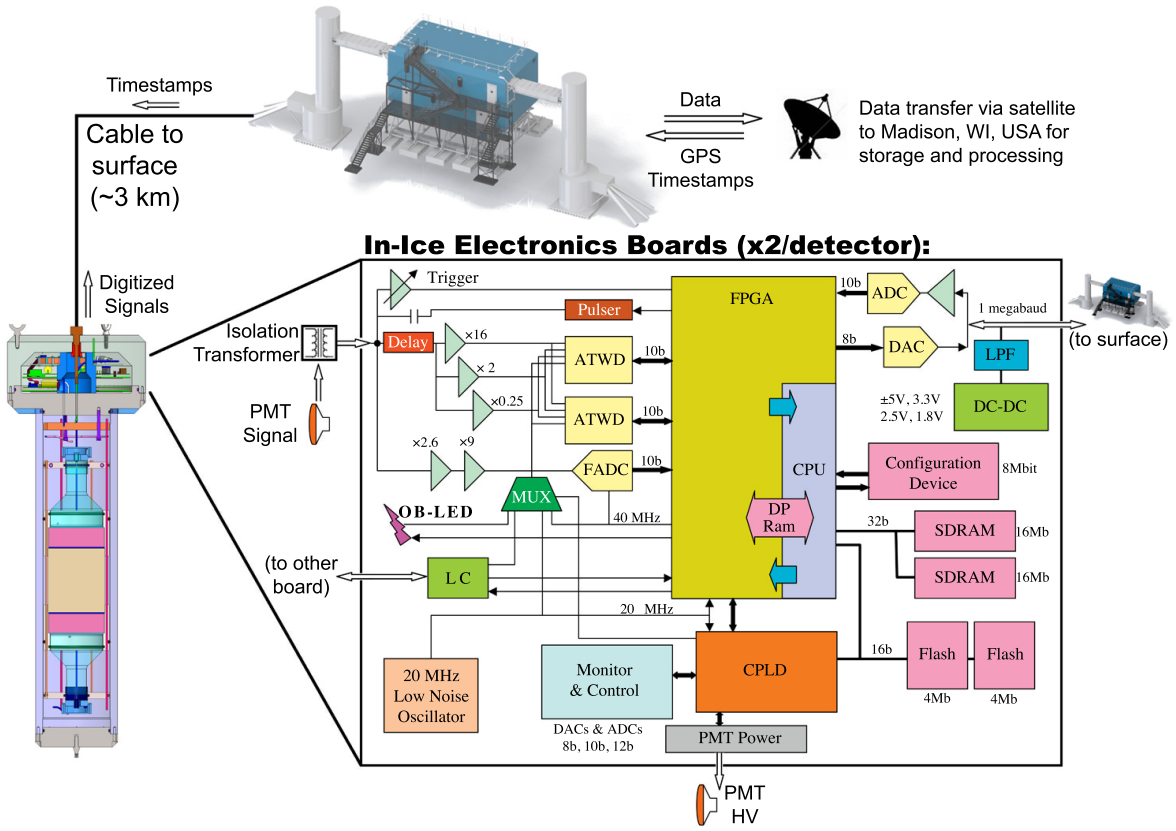

Figure 2: Block diagram of one DM-Ice17 detector and data transfer. The scintillation light is collected with two PMTs and read out by the two mainboards (DOM-MBs, described in Ref. [36]) located in the top portion of the pressure vessel. The waveforms are digitized, given a timestamp, and sent to a hub in the ICL through a twisted pair of copper wires. Data are sent via satellite to the data warehouse located at the University of Wisconsin–Madison. The DOM-MB is also responsible for controlling the trigger threshold and PMT HV, as well as monitoring relevant PMT and environmental parameters.

2.3. Location

DM-Ice17 is operating in Antarctica roughly 1 km from the geographic South Pole. It was co-deployed with IceCube during the construction season of the 2010/2011 austral summer. The two detectors were lowered into separate, water-filled holes, 2457 m deep and 60 cm in diameter, and permanently frozen into place. The two holes, drilled by Ice Cube's Enhanced Hot Water Drill, are separated by 545 m. The ice provides 2200 meters water equivalent of overburden.

Both detectors are deployed on IceCube strings, 7 m below the lowest Digital Optical Module (DOM). The IceCube array consists of 1 km^3 of glacial ice instrumented with 5160 DOMs distributed across 86 strings, with 324 additional DOMs on the surface of the ice as IceTop. One of the DM-Ice17 detectors, Det-1, is located near the center of the IceCube array at the bottom of DeepCore [37] on String-79 [38]. Det-2 is at the edge of the IceCube array on String-07 (see Fig. 3).

Though operating independently from IceCube, DM-Ice17 uses the same data acquisition software and GPS time stamps, providing opportunities to study coincident events with IceCube. The power and communication to the DM-Ice17 detectors are established through twisted pairs of copper wires connected to IceCube's main signal cables. They are controlled via hubs in the ICL located on the surface of the ice.

The South Pole ice at depths of 2100 – 2500 m is 70,000 – 100,000 years old [39, 40] and has contamination levels of $\sim 10^{-4}$ ppb for ^{238}U and ^{232}Th and ~0.1 ppb for $^{\text{nat}}$K [41, 42]. The primary source of contamination in the ice is the ~0.1 ppm of dust, consisting mostly of volcanic ash as was measured from ice core samples taken elsewhere in Antarctica. The age of the ice and the depth dependent contamination levels at particular depths at the the South Pole are correlated to those from the core sample with the optical measurements made by the IceCube collaboration [43]. The ^{238}U concen-

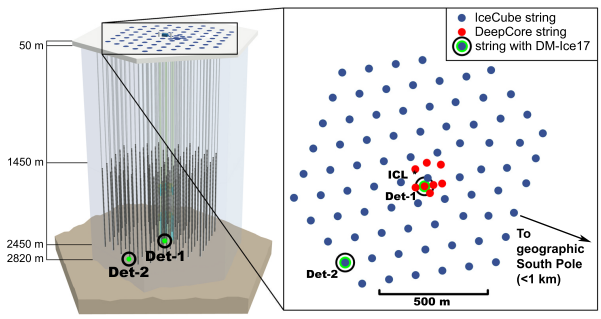

Figure 3: The locations of the DM-Ice17 detectors within the IceCube array, with Det-1 near the array center and Det-2 at the periphery. Both detectors are at a depth of 2457 m and are horizontally separated by 545 m. In the array top-view, blue points are IceCube strings, and red points are DeepCore strings.

tration was validated in Vostok ice core samples using inductively coupled plasma sector field mass spectrometry (ICP-SFMS).

The bedrock's contribution to the background of the detectors is negligible as they are shielded by over 300 m of ice. The environmental radon is also expected to be a negligible component of the total background as the detectors are completely encased in ice. The contamination levels of the water that fill the drilled holes were extracted for HPGe counting. Its simulated contribution to the region of interest for dark matter searches was found to be negligible (see Sec. 5.1).

3. Detector Deployment and Performance

3.1. Deployment

The detectors were shipped in November 2010, first by land to Los Angeles, CA, then by air to Christchurch, New Zealand. The detectors waited in Christchurch for two weeks on the surface before being flown to McMurdo Station in Antarctica. After a day in McMurdo, the detectors were flown to the South Pole Station.

The sealed pressure vessels were strapped down vertically into their custom-designed wooden shipping crates. A Shock Timer Plus 3D sensor (Instrumented Sensor Technology) was mounted inside each crate to monitor temperature, humidity, and mechanical shock during shipment. The large mass of the pressure vessel and additional layers of insulation mitigated thermal shock, and the suspension system mitigated mechanical shock to the crystals (see Sec. 2.1).

From Wisconsin to New Zealand, the temperature fluctuated about 15°C. Upon arrival at McMurdo Station, the temperature dropped from 25°C to -7°C over 15 hrs. At the South Pole, the temperature dropped 20°C in its first 7 hrs before stabilizing at the surface temperature of roughly -25°C. Prior to deployment, the detectors were relocated into the deployment tower and thermalized to 22°C; they were then rapidly lowered through the roughly -50°C air column at the top of the hole (50 – 100 m) into the 0°C water.

The fastest temperature change experienced by the crystal was expected when the detector hit the water and rapidly equilibrated to 0°C. Thermal shock during shipment was $< 6\,^{\circ}$C/hr prior to arrival at the South Pole. The largest mechanical shocks recorded were $< 10\ g$ for both Det-1 and Det-2, and were primarily during commercial shipment to New Zealand.

3.2. Freeze-In and Temperature Stability

The temperatures of the DOM-MBs are read out periodically by the DAQ (see Fig. 4). The temperature of the ice at this depth is roughly -18°C. The recorded temperatures are ~10°C warmer than their surroundings due to the ~2 W dissipated by the electronics [36]. The two DOM-MBs in the same pressure vessel are stacked on top of each other and rotated by 60°with respect to one another. The temperature sensor on the top DOM-MB sees a 2 – 3°C higher temperature than its partner (see Fig. 4) from the dissipated heat of the DC-DC converter located directly below it on the lower DOM-MB.

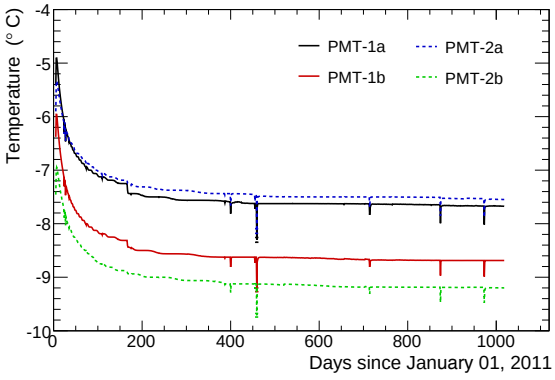

Figure 4: Temperature of DM-Ice17 mainboards since January 01, 2011, sampled every 2 sec through February 2011 and every 60 sec after (see Sec. 2.2). Two time constants are observed: a relative fast component (~10 days) that relates to the freeze-in process and a slower time constant (~50 days) as the heat accumulated in the ice surrounding the hole during drilling is dissipated. Discontinuities observed correspond to the PMT high voltage settings change (day ~160) and subsequent power outages (negative spikes).

As the ice froze and the detectors thermalized, the temperature decrease exhibited a fast and a slow expo-

nential time component. The fast freeze-in time constant (~10 days) is due to the water in the drilled hole freezing around the detector. The slow component of thermalization (~50 days) is thought to be due to the thermalization of the heat deposited in the nearby ice during the hot-water drilling process. The small drop on day ~160 corresponds to the change in the power dissipation in the mainboard when the PMT high voltage was lowered to the final run settings. The occasional dips in temperature correspond to power outages in either the ICL or the hub affecting the mainboards for more than an hour.

Since the beginning of the physics data run in July 2011, the temperature of the DM-Ice17 vessels has been stable with an RMS of 0.06°C. The crystal temperature is expected to be more stable than these DOM-MB measurements due to its larger thermal mass and increased distance from the electronics. The temperature dependence of the detector sensitivity is the subject of future studies and is not addressed here.

3.3. Hardware Stability

PMT high voltage is recorded periodically by the DAQ (see Sec. 2.2). The PMT voltages are stable to within fractions of a volt ($0.4-0.7\ V_{RMS}$), with the exception of PMT-2b. Despite a constant HV set-point and what appears to be a stable gain, PMT-2b shows random variation around the set point (~30 V_{pp}). This is likely an error related to the on-board HV power-supply controller or the HV monitoring hardware. No effects from this HV oscillation have been observed in PMT gain or single photoelectron (SPE) rate.

The gain stability of the PMTs was quantified by recording the position of the prominent 609 keV and 46.5 keV peaks in the uncalibrated energy spectrum (see Fig. 5). The 609 keV peak from ^{214}Bi exhibits a <2 % decrease in light collection over two years, which is smaller than the energy resolution and within the error of the energy calibration. The 46.5 keV peak from ^{210}Pb shows <2 % fluctuations and no significant trend during two years of monitoring.

The total coincident event rates are ~2.5 Hz and show a gradual decrease with time (0.027 Hz/yr for Det-1 and 0.013 Hz/yr for Det-2). No variation with time is observed in the PMT trigger thresholds extracted from dark noise (non-coincident) data runs.

3.4. Detector Livetime

DM-Ice17 took data nearly continuously, with a total livetime of 98.94 % (Det-1) and 98.92 % (Det-2) over the course of the data taking period presented here. The downtime is primarily from 10 extended (> 1 hour) interruptions due to power outages, test runs, and DAQ errors. Normal uninterrupted data sets achieve a ~99.75 % livetime, with small downtime introduced as the DAQ transitions between runs. A ~1 ms deadtime after each event introduces an additional ~0.25 % downtime (~2.5 Hz event rate).

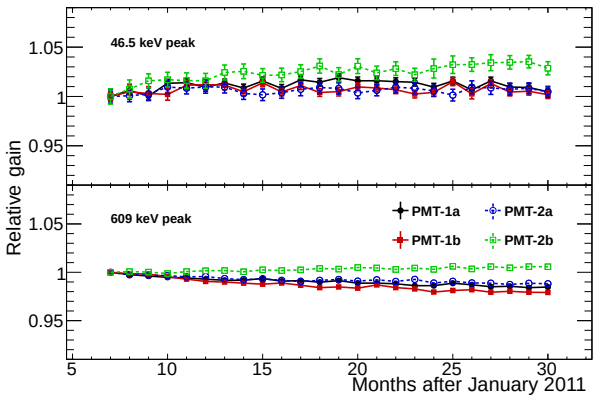

Figure 5: Gain stability of PMTs using the 46.5 keV ^{210}Pb (top) and 609 keV ^{214}Bi (bottom) gamma peaks as a reference. Gain variations are less than the resolution of the detectors at both energies (~3 % at 609 keV and ~10 % at 46.5 keV).

4. Detector Response

4.1. Data Processing and Calibration

Events passing the ~0.25 photoelectron trigger threshold and 800 ns coincidence window requirements are digitized at the DOM-MB in the ice (see Sec. 2.2). The digitized waveforms are then sent to the hub in the ICL and compiled into 1 hour runs. The data are transmitted via satellite to the University of Wisconsin–Madison for processing.

Offline data processing consists of waveform corrections and energy calibration. The waveform is first baseline adjusted and then corrected for the frequency response of the passive electronic components.

The energy calibration begins by integrating the entire corrected waveform (~600 ns for ATWD). The resulting spectrum for each PMT is converted into keV_{ee} using known internal contamination lines (^{40}K, ^{60}Co, ^{125}I, ^{232}Th-chain, and ^{238}U-chain) in order to account for PMT gain and non-linearity. The final energy spectra, presented here for Det-1 (see Fig. 6), are produced by combining the light collected in both PMTs on a single crystal for each event. The calibrated energies are

in electron-equivalent keV ($\mathrm{keV_{ee}}$), unless otherwise stated.

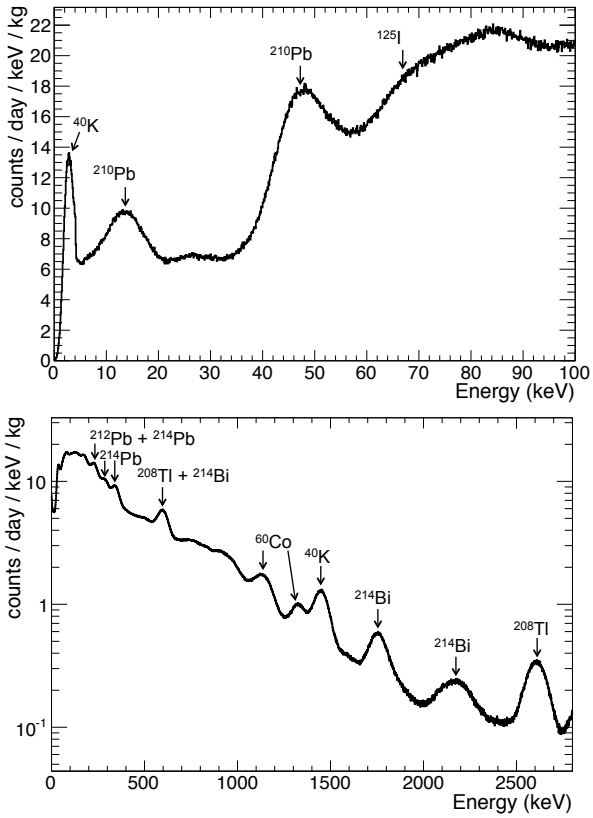

Figure 6: The Det-1 calibrated energy spectrum with prominent lines identified. ATWD0 (the highest gain channel) is used for the low-energy plot (top), and ATWD1 is used for the high-energy plot (bottom); the spectra from these two channels overlap well from 100–1000 keV. The non-linear response of NaI requires that separate calibrations be applied for the two energy regions. All lines depicted are included in calibration fits and energy resolution analysis.

Each channel is optimized for a different energy range based on its gain and saturation energy. ATWD0 is useful for 0 – 1000 keV, ATWD1 for 100 – 5000 keV, and ATWD2 > 1000 keV. The longer FADC digitization window carries important timing information, but the FADC energy spectrum is not used in present analyses.

The non-linear light response of NaI requires that two different energy calibrations be applied to the data. An extrapolation of the high-energy linear calibration results in a negative intercept, consistent with behavior observed in literature [44–47]. Due to the higher light yield at low energy, a separate linear low-energy calibration is applied below 100 keV.

4.2. Cosmogenic Isotopes

A measurement of the decay rate of short-lived cosmogenically-activated isotopes provides a robust verification of the energy calibration. The duration spent at each location and elevation was tracked during construction and deployment for major detector components, and the expected activation was simulated in ACTIVIA [48] (NaI crystal) or scaled from literature values (steel pressure vessel) [49]. The resulting isotopes were propagated through the detector using the DM-Ice17 Geant4 simulation package. In DM-Ice17, ^{125}I from ^{127}I activated in the crystal and ^{54}Mn from ^{56}Fe in the pressure vessel provide the clearest cosmogenic signal due to their energies and half-lives.

Cosmogenic ^{125}I is observed in the DM-Ice17 data (see Fig. 7) exhibiting the expected peaks at 37.7 and 65.3 keV resulting from a combination of gammas and x-rays. Using one-month intervals of data, the measured half-life of this isotope is 59.4 ± 2.7 days, consistent with the quoted 59.40 ± 0.01 day half-life of ^{125}I [50]. The ^{125}I activity, extrapolated back to deployment, was determined to be 1151 ± 118 decays/day/kg. Simulation using ACTIVIA estimated an activity of 407 decays/day/kg. This discrepancy may be attributed to uncertainty in the activation calculation and scaling factors applied; future measurements on test crystals may reduce uncertainty in the activation rate.

The gamma line from ^{54}Mn is also observed in the data (see Fig. 7) at a calibrated energy of 836.1 ± 3.0 keV, consistent with the literature value of 834.848 ± 0.003 keV [50]. The measured half-life is consistent with the tabulated value of 312 days, although accurate measurement has not been made due to low statistics. The ^{54}Mn activity, extrapolated back to deployment assuming the literature half-life, was determined to be 51700 ± 6500 decays/day (corrected for detection efficiency of decays in the pressure vessel found from Geant4 simulation, see Sec. 5.2). Simulation based on literature activation rates estimated an activity of 41850 ± 4650 decays/day (error only from activation rate measurement) from the pressure vessel, in good agreement given additional uncertainty in the scaling factors.

4.3. Energy Resolution and Light Yield

The energy resolution of the DM-Ice17 detectors (see Fig. 8) is measured by fitting a Gaussian plus linear background around the peak of internal contamination lines. It is comparable to that of NaI crystals of similar size from NaIAD [33] and DAMA/LIBRA [51] as well as to a small 2” crystal reported in [52]. DAMA

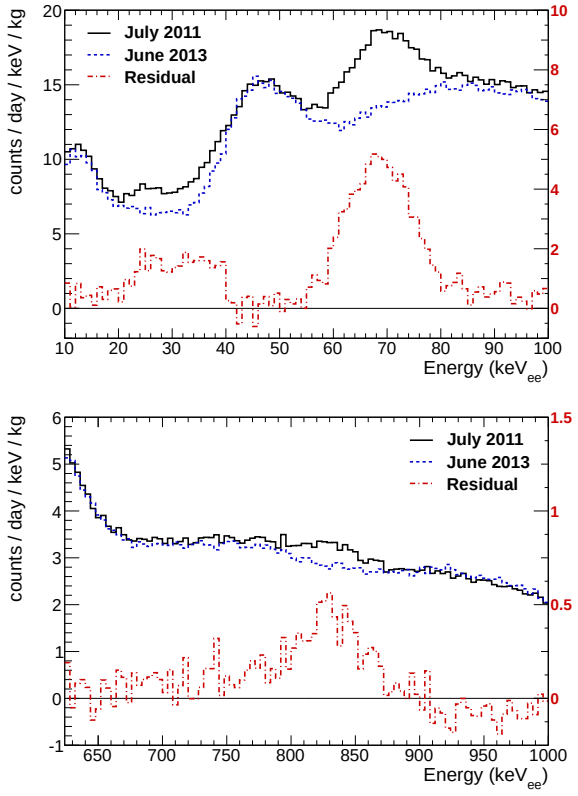

Figure 7: Evidence for cosmogenic activation in Det-1 spectra from July 2011 (black, solid), June 2013 (blue, dashed), and residual (red, dot-dashed, rescaled axis). The top figure shows the decay of lines (37.7 and 65.3 keV) from cosmogenic ^{125}I in the crystal. The bottom figure shows the decay of the 834.8 keV gamma line from cosmogenic ^{54}Mn in the pressure vessel.

reports their energy resolution separately for above and below ~80 keV as they use two different ADC channels for the two energy regions, resulting in the discontinuity shown in Fig. 8. The resolution of the 3 keV peak from ^{40}K has large error due to the uncertainty in the cut efficiency (see Sec. 6). The ~12 keV peak from ^{210}Pb is broadened due to the many (> 10) x-rays that make up that peak. The 2204 keV peak from ^{214}Bi is broadened by contributions from ^{208}Tl decay.

Single photoelectron (SPE) events are collected by relaxing the two-PMT coincidence trigger requirement during regularly scheduled dark noise runs. The light yield is measured by comparing the peak location of the 65.3 keV calibration line from ^{125}I to that of the SPE peak. The measured light yields are 5.9 ± 0.1 pe/keV and 4.3 ± 0.1 pe/keV for Det-1 and Det-2 respectively.

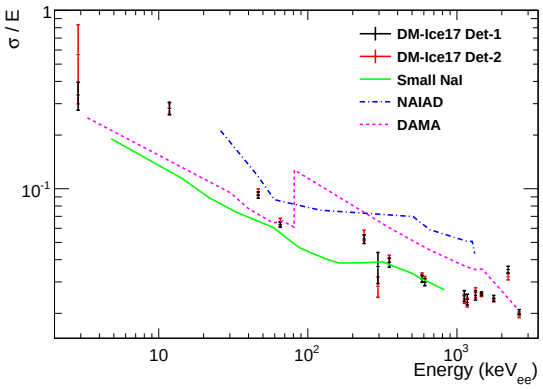

Figure 8: Energy resolution of Det-1 (black) and Det-2 (red) compared to a DAMA crystal (magenta, dashed) [51], NaIAD detector DM77 (blue, dot-dashed) [33], and 2" NaI detector (green, solid) [52]. The discontinuity in the DAMA resolution is due to switching ADC channels. The internal contamination lines were fit with a Gaussian plus linear background, the quantity σ is the standard deviation of the fit and the error bar is the fitted parameter error.

4.4. *Pulse Shape Discrimination for alphas*

Alpha events can be separated from gammas via pulse shape discrimination. Alphas produce shorter scintillation waveforms than gammas, leading to observable differences in the behavior in the tail of the recorded waveforms. A comparison of average alpha and gamma waveforms, as recorded in the ATWD1 channel, is shown in Fig. 9. Longer time windows are available in the FADC channel; however, the pulses are saturated for MeV events and therefore are not used in this analysis.

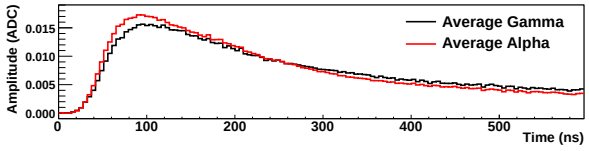

Figure 9: An average of $O(100)$ normalized gamma and alpha waveforms as recorded in the ATWD1 channel of PMT-1a. Particle identification is possible through pulse-shape discrimination.

A parameter referred to as the mean time (τ) quantifies the decay behavior of waveforms and is defined numerically as:

$$\tau = \frac{\sum_{n=n_0}^{n_0+99} (n - n_0)\,(ADC_n)}{\sum_{n=n_0}^{n_0+99} ADC_n} \qquad (4.1)$$

where ADC_n refers to the charge collected in the nth time bin of the waveform and n_0 is the time when the waveform first reached 50% of its maximum. To account for variations in the time between the start of scintillation and the start of the recorded waveform, the mean time calculation begins at n_0 and samples 100 bins.

Above 2000 keV, gamma and alpha separation via the mean time nears 100% (see Fig. 10). Less than one misidentified event in the primary region of overlap between gammas and alphas (2500 – 3500 keV) is expected for the 24 months of data presented here.

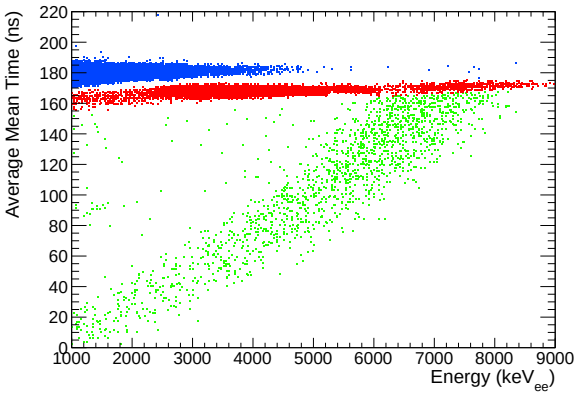

Figure 10: Waveform mean time values from Det-1 demonstrating separation between electron recoils (blue, $\tau \approx 180$ ns) and alpha events (red, $\tau \approx 165$ ns). The diagonal band at lower τ (green) is composed of Bi-Po events (see Sec. 5.3).

5. Background Analysis

5.1. External Backgrounds

The energy spectra for 100 – 2000 keV from the DM-Ice17 data shows good agreement with simulations based on radioassays of components and data-based estimates (see Fig. 11). The background levels from the two detectors are similar, and the spectrum from Det-1 is shown as representative of the two. The contamination levels used in the simulation are listed in Tab. 2 for the NaI crystals and in Tab. 1 for all other components.

During construction, excess stock from the stainless steel pressure vessel, PTFE light reflectors, and copper plates, as well as silicone gel and grease for optical coupling, were set aside to be measured at SNOLAB's low-background counting facility [35]. Samples of the drill water were taken just prior to heating and recirculating through the pressurized nozzle. Eleven water samples were taken at varying depths on eight separate holes.

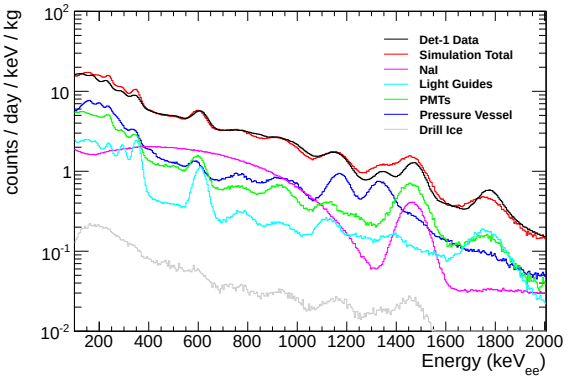

Figure 11: The energy spectrum in keV$_{ee}$ from Det-1 (black) and simulation total (red). Simulated contributions from the NaI crystal and nearby components based on data-based estimates and radioassays are also shown separately (see Tab. 1 and Tab. 2).

The contamination levels measured in the extracted drill water showed no significant dependence on the depth or the order in which the holes were drilled; Tab. 1 shows the average measured contamination.

The contamination levels for the quartz light guides were taken from the 'Spectrosil B silica rod' values on the ILIAS database [53]. The PMT levels for the low-background 9390 were provided in the ETL datasheet. The contamination levels of the NaI crystals were derived from simulation comparison to data features (see Sec. 5.2). The glacial ice contamination is estimated using the ice core data and optical measurements from IceCube, as described in [31]. The contributions from PTFE, silicone gel, drill ice, and glacial ice were simulated and found to be negligible.

Detector and background modeling were performed using the 4.9.5 release of the Geant4 software package [54, 55]. The physics list was modeled off the "rdecay02" example code, which utilizes the Livermore processes for atomic deexcitation.

5.2. Backgrounds from NaI Crystals

The alpha lines between 4 and 7.5 MeV were used to measure the ^{238}U and ^{232}Th contaminations in the NaI(Tl) crystals. The events in these lines are expected to be dominated by those occurring in the bulk of the NaI(Tl) crystals. The observed spectrum obtained from each PMT is compared to Geant4-based simulation and contamination levels are evaluated by matching the relative heights of the peaks (see Fig. 12). Both ^{238}U and ^{232}Th chains appear to be broken, as described in Tab. 2.

Table 1: Contamination levels of DM-Ice17 detector components in mBq/kg. Quartz measurements taken from ILIAS database for 'Spectrosil B' silica rod [53], and PMT levels from the ETL 9390B datasheet. Components that were measured specifically for this experiment at SNOLAB [35] are indicated by *. Components not shown in Fig. 11 are denoted by †.

Material	^{40}K	^{232}Th	^{238}U (^{234}Th)	^{238}U (^{226}Ra)	^{235}U	^{60}Co
Quartz Light Guides	0.50 ± 0.03	< 4.9	< 12		–	–
ETL 9390B PMT	9000	1000	1000		–	–
Pressure Vessel *	13.77 ± 6.38	6.49 ± 0.96	118.31 ± 60.11	2.28 ± 0.72	8.79 ± 1.68	7.19 ± 0.82
Drill Ice *	3.71 ± 1.36	0.55 ± 0.17	6.69 ± 3.02	0.39 ± 0.14	0.38 ± 0.21	0.12 ± 0.05
Optical Gel * †	39.50 ± 18.60	< 0.12	2.08 ± 1.10	38.50 ± 61.00	0.96 ± 1.30	0.32 ± 0.42
Teflon * †	0.34 ± 5.09	0.52 ± 0.44	< 0.41	24.46 ± 21.37	1.92 ± 0.72	< 0.089
Copper * †	< 5.13	< 1.22	0.17 ± 0.92	< 0.67	3.56 ± 1.79	< 0.12
Glacial Ice †	$\sim 3\times10^{-3}$	$\sim 4\times10^{-3}$	$\sim 10^{-3}$		–	–

The cause of the shoulders observed in the peaks of the alpha spectrum is under investigation.

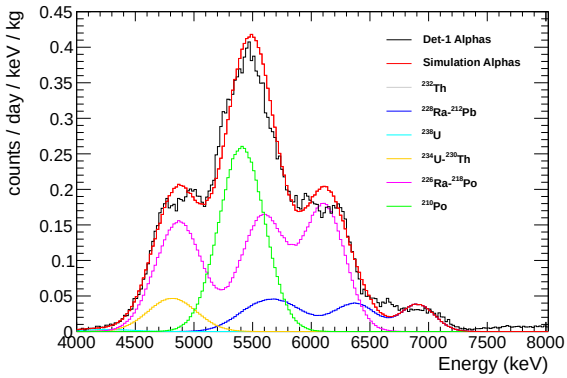

Figure 12: The energy spectrum in the alpha region of ^{238}U and ^{232}Th and chains in the NaI(Tl) crystal as measured with PMT-1b of Det-1 (black) and simulation (red). The energy scale shown takes into account the correction from the gamma-calibrated spectrum using the quenching factor (see text). Comparison to simulation yields contaminant estimates of the ^{238}U and ^{232}Th and chains in the crystal as listed in Tab. 2.

The light yield of the NaI(Tl) detectors from alpha interactions differ from those induced by gammas. The measured alpha quenching factors are $\alpha/\gamma = 0.435 + 0.039E_\alpha(MeV)$ and $\alpha/\gamma = 0.47 + 0.034E_\alpha(MeV)$ for Det-1 and Det-2, respectively, consistent with those reported in [51].

For short-lived isotopes ^{214}Po (^{238}U-chain) and ^{212}Po (^{232}Th-chain), activities are estimated by Bi-Po events from data (see Sec. 5.3). This analysis supports the contamination levels derived from the alpha spectrum.

Table 2: Contamination in the DM-Ice17 NaI crystals as determined by simulation comparison to spectra. The activity levels in the two detectors are consistent within the ~30% error of these numbers. Both ^{238}U and ^{232}Th chains were observed to be broken.

Isotope	Subchain	Activity (mBq/kg)
^{40}K		20
^{129}I		1
^{232}Th	^{232}Th	0.01
	^{228}Ra – ^{208}Tl	0.16
^{238}U	^{238}U – ^{234}Pa	0.017
	^{234}U – ^{230}Th	0.14
	^{226}Ra – ^{214}Po	0.91
	^{210}Pb – ^{210}Po	1.47

The contamination levels of ^{40}K and ^{129}I were measured by using their continuous beta spectra with endpoints at ~1311 keV and ~154 keV respectively to match the simulation with the data.

5.3. Bi-Po Events

For short-lived isotopes in a decay chain, it is possible to observe parent and daughter decays in the same waveform (see Fig. 13). In DM-Ice17, this most commonly occurs when ^{212}Bi decays into ^{212}Po ($t_{1/2} = 299 \pm 2$ ns) [50]. A secondary contribution to the double-event population comes from ^{214}Bi decays into ^{214}Po ($t_{1/2} = 164.3 \pm 0.2\ \mu s$). The events from these processes are referred to as Bi-Po events.

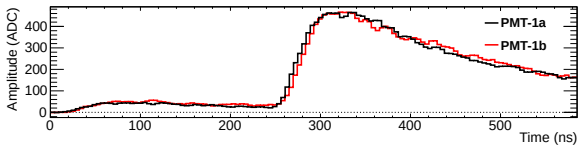

Figure 13: An example Bi-Po waveform recorded in the ATWD1 channels of PMT-1a (black) and PMT-1b (red). The first peak is the beta decay from ^{212}Bi, and the second larger peak is from the alpha decay of ^{212}Po ($t_{1/2} = 299$ ns).

Because the high-energy alpha event is delayed, a larger portion of the waveform tail is truncated. This loss results in a suppression of the calculated mean time and calibrated energy of these events (see Fig. 10).

For individual events of this nature, the time between the gamma and alpha decays is recorded. The distribution of these decay times contains an exponential component due to ^{212}Bi and a flat continuum due to ^{214}Bi (see Fig. 14). The exponential component of the fit yields a half-life of 298.6 ± 4.0 ns, verifying ^{212}Po as the source of these events.

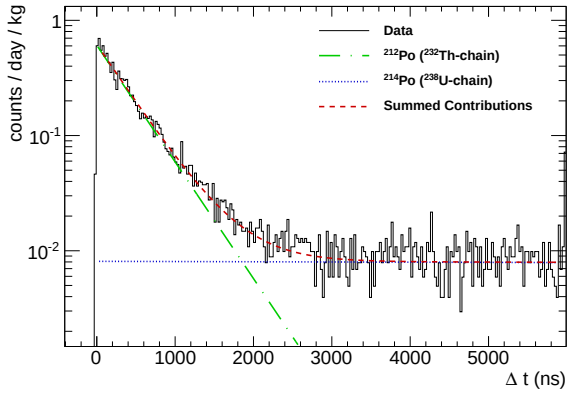

Figure 14: The time between decays of Bi-Po events in PMT-1a. Exponential fit component from ^{212}Bi decay (green, dot-dashed), flat continuum from ^{214}Bi decay (blue, dotted), and composite fit (red, dashed) overlain on data (black, solid).

This analysis and the alpha-peaks analysis yield similar results for the level of contamination observed in the NaI crystals (see Tab. 3).

6. Low Energy Region

The raw energy spectrum below 25 keV is shown in Fig. 15. The raw spectrum (shown in solid black line) below 20 keV is dominated by noise comprised of three

Table 3: Contamination levels (in μBq/kg) of ^{212}Bi (^{232}Th-chain) and ^{214}Bi (^{238}U-chain) in the DM-Ice17 NaI crystals derived from Bi-Po data analysis and simulation.

Isotope	Bi-Po Analysis		Simulation
	Det-1	Det-2	
^{212}Bi	125.7 ± 0.9	124.5 ± 0.9	160
^{214}Bi	892 ± 18	890 ± 18	910

main components: electromagnetic interference (EMI), thin pulses, and the accidental coincidence of single photoelectrons (SPE) of the two PMTs. Their distinctive pulse shapes are used to identify them; the spectrum after cuts is shown in gray. Thin pulses are the dominant

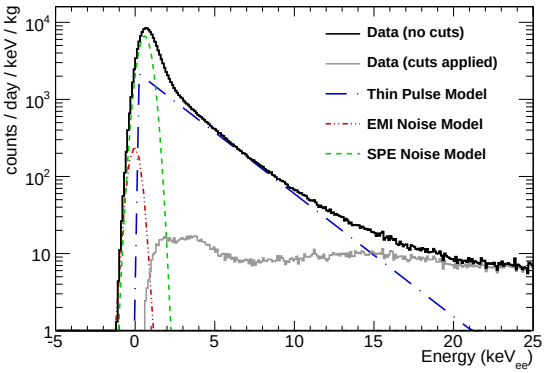

Figure 15: The low energy spectrum of Det-1 before (black, solid) and after (gray, solid) analysis cuts. Models of the noise from thin pulses (blue, dot-dashed), electromagnetic interference (red, dot-dot-dashed), and correlated single photoelectrons (green, dashed) are shown.

noise source in the region of interest (2 – 20 keV), while EMI and SPE noise dominate below 1 keV. The waveforms associated with signal and these sources of noise are shown in Fig. 16.

EMI events occur when the mainboards are periodically queried for their monitoring information (see Sec. 2.2) and are well correlated in timing to the monitoring queries. EMI events are characterized by their oscillatory waveforms (see Fig. 16(d)), which can be distinguished from signal events by summing the square of the second derivative. The parameter used to cut the EMI events is:

$$\sum_{n=0}^{N} \left[(ADC_{n+1} - ADC_n) - (ADC_n - ADC_{n-1}) \right]^2, \quad (6.1)$$

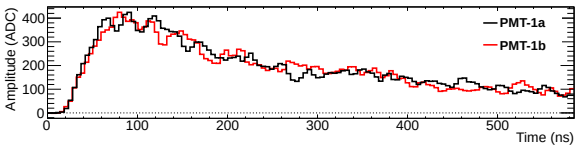

(a) High-energy scintillation event

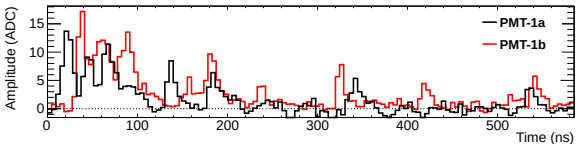

(b) Low-energy scintillation event

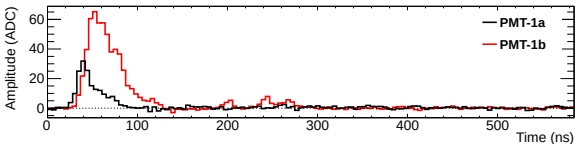

(c) Thin pulses

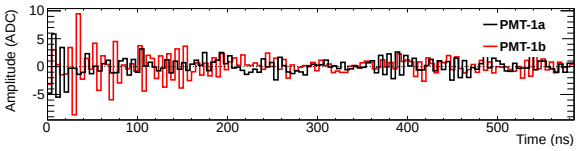

(d) Electromagnetic interference

Figure 16: Example coincident waveforms of different event types recorded by PMT-1a (black) and PMT-1b (red). Waveforms (a) and (b) are signal events at high and low energies at ~700 keV and ~10 keV respectively. Waveforms (c) and (d) are noise events present in the raw data.

where ADC_n is the nth time bin in the recorded waveform. A cut using this parameter and energy removes 99.98% of EMI events while preserving 99.99% of non-EMI events. Additionally, the highest observed energy for an EMI event is 1.6 keV. The status query interval was reduced from 2 sec to 60 sec in February 2012.

Thin pulse events are characterized by tall, narrow waveforms (see Fig. 16(c)); most of the light is collected within 100 ns, on a time scale much faster than the decay time of NaI scintillation (~600 ns at -20°C [56]). The ratio of the pulse area to the pulse height provides discrimination between thin pulses and scintillation events above 4 keV. At lower energies, the number of "peaks" observed in the recorded waveform is also used to distinguish scintillation-like events from thin pulse and SPE: thin- and SPE-pulses typically only have one peak in the recorded waveforms whereas scintillation events above 2 keV will have at least three or more in each PMT (see Fig. 16(b)). The energy spectrum of thin pulses from 4 – 20 keV is exponential, and is modeled to persist back to 0 keV in Fig. 15. The thin pulses are suspected to originate from Cherenkov light in the quartz or PMT windows. Their timing characteristics are similar to noise pulses observed in other NaI detectors including those of DAMA/LIBRA [51]. Understanding their contribution to the signal region and their stability is critical for annual modulation studies.

Correlated SPE events comprise the final major component of noise in DM-Ice17. This class of noise events form a gaussian peak with a mean at $\mu = 0.6$ keV and width of $\sigma = 0.4$ keV, as shown in green-dashed line in Fig. 15. The shape matches the SPE spectrum of the data taken without imposing the two-PMT coincidence requirement, however the rate is about two orders of magnitude higher than that expected from random coincidences between uncorrelated single photo electrons from the two PMTs. This may indicate inadequate modeling of the thin-pulses or electronics noise, however these events are eliminated from the data with the peak number cut.

After applying a cut on the number of peaks, several low energy features are visible in the remaining data: a broad peak around 14 keV, peak at 3 keV, and remnant noise below 2 keV. The features are validated against Geant4 simulations, as shown in Fig. 17. The broad peak at 14 keV can be attributed to a combination of ^{210}Pb on the surface of the copper encapsulation and ^{238}U-chain contaminants in the quartz light guides. The 3 keV peak is from Auger electrons and x-rays from ^{40}K decays in the crystal. A background of 7.9 ± 0.4 counts/day/keV/kg is observed between 6.5 – 8 keV, below which the spectrum is dominated by the ^{40}K peak.

7. Conclusions

DM-Ice17 was successfully constructed and deployed in December 2010. The data presented here from July 2011 – June 2013 demonstrate the excellent environmental conditions, including temperature stability with RMS of 0.06°C. A livetime of ~99 % was achieved by the detectors during this data period.

It has been shown for the first time that low-background scintillator detectors can be remotely calibrated and operated under the ice at the South Pole. This has promising implications for future dark matter searches in the Southern Hemisphere.

The background observed in DM-Ice17 is dominated by those produced by the internal contamination in the crystal assemblies. Data are in good agreement with simulation of expected contaminants in de-

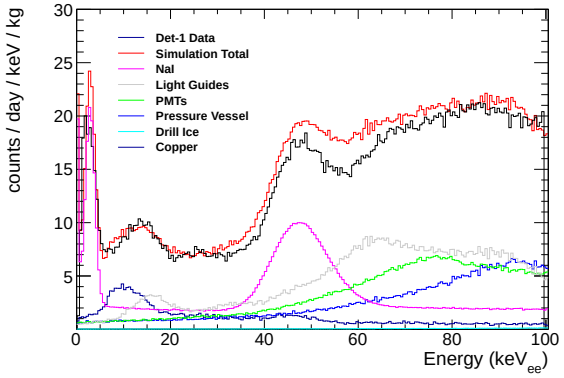

Figure 17: The energy spectrum of DM-Ice17 Det-1 (black) and simulation total (red). Simulated contributions from nearby detector components are also shown. The spectrum below 20 keV consists primarily of the 3 keV peak from ^{40}K and a 14 keV peak from ^{210}Pb on the surface of the copper encapsulation and ^{238}U-chain contaminants in the quartz light guides. The background observed between 6.5 – 8 keV is 7.9 ± 0.4 counts/day/keV/kg.

tector components, and contributions from environmental backgrounds have been shown to be negligible. In the 6.5 – 8.0 keV region, a background rate of 7.9 ± 0.4 counts/day/keV/kg is observed, consistent with expected backgrounds. The energy region of interest between 2 – 6 keV is dominated by the events from ^{40}K peak at 3 keV. Studies of the low-energy region, including a modulation analysis and veto capabilities through coincidence with IceCube will be discussed in a separate paper.

8. Acknowledgments

We thank the IceCube collaboration and construction team for their support in the successful deployment of the detector and on-going detector monitoring and data management. We thank the support from SNOLAB for their efforts on the low background measurements, and STFC and the Boulby mine company CPL for support of low background measurements of NaI. This work was supported by the NSF Grants No. PLR-1046816 and PHY-1151795, Wisconsin IceCube Particle Astrophysics Center, the Wisconsin Alumni Research Foundation, Yale University, the National Science and Engineering Research Council of Canada, and Fermilab, operated by Fermi Research Alliance, LLC under Contract No. DE-AC02-07CH11359 with the United States Department of Energy. W. P. and A. H. are supported by the DOE/NNSA Stewardship Science Graduate Fellowship (Grant No. DE-FC52-08NA28752) and NSF Graduate Research Fellowship (Grant No. DGE-1256259) respectively.

References

[1] P. Ade, et al., Planck 2013 results. XVI. Cosmological parametersarXiv:1303.5076.

[2] G. Bertone, D. Hooper, J. Silk, Particle dark matter: Evidence, candidates and constraints, Phys.Rept. 405 (2005) 279–390. arXiv:hep-ph/0404175, doi:10.1016/j.physrep.2004.08.031.

[3] S. Faber, J. Gallagher, Masses and mass-to-light ratios of galaxies, Ann.Rev.Astron.Astrophys. 17 (1979) 135–183. doi:10.1146/annurev.aa.17.090179.001031.

[4] G. Steigman, M. S. Turner, Cosmological Constraints on the Properties of Weakly Interacting Massive Particles, Nucl.Phys. B253 (1985) 375. doi:10.1016/0550-3213(85)90537-1.

[5] M. W. Goodman, E. Witten, Detectability of Certain Dark Matter Candidates, Phys.Rev. D31 (1985) 3059. doi:10.1103/PhysRevD.31.3059.

[6] R. Gaitskell, Direct detection of dark matter, Ann.Rev.Nucl.Part.Sci. 54 (2004) 315–359. doi:10.1146/annurev.nucl.54.070103.181244.

[7] A. Drukier, K. Freese, D. Spergel, Detecting Cold Dark Matter Candidates, Phys.Rev. D33 (1986) 3495–3508. doi:10.1103/PhysRevD.33.3495.

[8] K. Freese, J. A. Frieman, A. Gould, Signal Modulation in Cold Dark Matter Detection, Phys.Rev. D37 (1988) 3388. doi:10.1103/PhysRevD.37.3388.

[9] S. Chang, A. Pierce, N. Weiner, Momentum Dependent Dark Matter Scattering, JCAP 1001 (2010) 006. arXiv:0908.3192, doi:10.1088/1475-7516/2010/01/006.

[10] R. Bernabei, P. Belli, F. Cappella, R. Cerulli, F. Montecchia, et al., Dark matter particles in the Galactic halo: Results and implications from DAMA/NaI, Int.J.Mod.Phys. D13 (2004) 2127–2160. arXiv:astro-ph/0501412, doi:10.1142/S0218271804006619.

[11] R. Bernabei, P. Belli, F. Cappella, V. Caracciolo, S. Castellano, et al., Final model independent result of DAMA/LIBRA-phase1arXiv:1308.5109.

[12] C. Aalseth, et al., CoGeNT: A Search for Low-Mass Dark Matter using p-type Point Contact Germanium Detectors, Phys.Rev. D88 (2013) 012002. arXiv:1208.5737, doi:10.1103/PhysRevD.88.012002.

[13] C. Aalseth, P. Barbeau, J. Colaresi, J. Collar, J. D. Leon, et al., Search for An Annual Modulation in Three Years of CoGeNT Dark Matter Detector DataarXiv:1401.3295.

[14] G. Angloher, M. Bauer, I. Bavykina, A. Bento, C. Bucci, et al., Results from 730 kg days of the CRESST-II Dark Matter Search, Eur.Phys.J. C72 (2012) 1971. arXiv:1109.0702, doi:10.1140/epjc/s10052-012-1971-8.

[15] R. Agnese, et al., Dark Matter Search Results Using the Silicon Detectors of CDMS II, Phys.Rev.Lett.arXiv:1304.4279.

[16] D. Akerib, et al., First results from the LUX dark matter experiment at the Sanford Underground Research FacilityarXiv:1310.8214.

[17] E. Aprile, et al., Dark Matter Results from 100 Live Days of XENON100 Data, Phys.Rev.Lett. 107 (2011) 131302. arXiv:1104.2549, doi:10.1103/PhysRevLett.107.131302.

[18] J. Angle, et al., A search for light dark matter in XENON10 data, Phys.Rev.Lett. 107 (2011) 051301. arXiv:1104.3088, doi:10.1103/PhysRevLett.107.051301.

[19] Z. Ahmed, et al., Results from a Low-Energy Analysis of the CDMS II Germanium Data, Phys.Rev.Lett. 106 (2011) 131302. arXiv:1011.2482, doi:10.1103/PhysRevLett.106.131302.

[20] E. Armengaud, et al., Final results of the EDELWEISS-II WIMP search using a 4-kg array of cryogenic germanium detectors with interleaved electrodes, Phys.Lett. B702 (2011) 329–335. arXiv:1103.4070, doi:10.1016/j.physletb.2011.07.034.

[21] S. Kim, H. Bhang, J. Choi, W. Kang, B. Kim, et al., New Limits on Interactions between Weakly Interacting Massive Particles and Nucleons Obtained with CsI(Tl) Crystal Detectors, Phys.Rev.Lett. 108 (2012) 181301. arXiv:1204.2646, doi:10.1103/PhysRevLett.108.181301.

[22] E. Behnke, J. Behnke, S. Brice, D. Broemmelsiek, J. Collar, et al., Improved Limits on Spin-Dependent WIMP-Proton Interactions from a Two Liter CF3I Bubble Chamber, Phys.Rev.Lett. 106 (2011) 021303. arXiv:1008.3518, doi:10.1103/PhysRevLett.106.021303.

[23] V. Lebedenko, et al., Limits on the spin-dependent WIMP-nucleon cross-sections from the first science run of the ZEPLIN-III experiment, Phys.Rev.Lett. 103 (2009) 151302. arXiv:0901.4348, doi:10.1103/PhysRevLett.103.151302.

[24] M. Barnabe-Heider, et al., Improved spin dependent limits from the PICASSO dark matter search experiment, Phys.Lett. B624 (2005) 186–194. arXiv:hep-ex/0502028, doi:10.1016/j.physletb.2005.08.021.

[25] A. V. Belikov, J. F. Gunion, D. Hooper, T. M. Tait, CoGeNT, DAMA, and Light Neutralino Dark Matter, Phys.Lett. B705 (2011) 82–86. arXiv:1009.0549, doi:10.1016/j.physletb.2011.09.081.

[26] P. Draper, T. Liu, C. E. Wagner, L.-T. Wang, H. Zhang, Dark Light Higgs, Phys.Rev.Lett. 106 (2011) 121805. arXiv:1009.3963, doi:10.1103/PhysRevLett.106.121805.

[27] M. R. Buckley, D. Hooper, T. M. Tait, Particle Physics Implications for CoGeNT, DAMA, and Fermi, Phys.Lett. B702 (2011) 216–219. arXiv:1011.1499, doi:10.1016/j.physletb.2011.06.090.

[28] D. Tucker-Smith, N. Weiner, Inelastic dark matter, Phys.Rev. D64 (2001) 043502. arXiv:hep-ph/0101138, doi:10.1103/PhysRevD.64.043502.

[29] D. Hooper, J. Collar, J. Hall, D. McKinsey, C. Kelso, A Consistent Dark Matter Interpretation For CoGeNT and DAMA/LIBRA, Phys.Rev. D82 (2010) 123509. arXiv:1007.1005, doi:10.1103/PhysRevD.82.123509.

[30] P. Gondolo, G. Gelmini, Compatibility of DAMA dark matter detection with other searches, Phys.Rev. D71 (2005) 123520. arXiv:hep-ph/0504010, doi:10.1103/PhysRevD.71.123520.

[31] J. Cherwinka, et al., A Search for the Dark Matter Annual Modulation in South Pole Ice, Astropart.Phys. 35 (2012) 749–754. arXiv:arXiv:1106.1156, doi:10.1016/j.astropartphys.2012.03.003.

[32] A. Achterberg, et al., First Year Performance of The IceCube Neutrino Telescope, Astropart.Phys. 26 (2006) 155–173. arXiv:astro-ph/0604450, doi:10.1016/j.astropartphys.2006.06.007.

[33] B. Ahmed, G. Alner, H. Araujo, J. Barton, A. Bewick, et al., The NAIAD experiment for WIMP searches at Boulby mine and recent results, Astropart.Phys. 19 (2003) 691–702. arXiv:hep-ex/0301039, doi:10.1016/S0927-6505(03)00115-4.

[34] G. Alner, et al., Limits on WIMP cross-sections from the NAIAD experiment at the Boulby Underground Laboratory, Phys.Lett. B616 (2005) 17–24. arXiv:hep-ex/0504031, doi:10.1016/j.physletb.2000.09.001.

[35] I. Lawson, B. Cleveland, Low background counting at SNOLAB, AIP Conf.Proc. 1338 (2011) 68–77. doi:10.1063/1.3579561.

[36] R. Abbasi, et al., The IceCube Data Acquisition System: Signal Capture, Digitization, and Timestamping, Nucl.Instrum.Meth. A601 (2009) 294–316. arXiv:arXiv:0810.4930, doi:10.1016/j.nima.2009.01.001.

[37] R. Abbasi, et al., The Design and Performance of IceCube DeepCore, Astropart.Phys. 35 (2012) 615–624. arXiv:1109.6096, doi:10.1016/j.astropartphys.2012.01.004.

[38] T. K. Gaisser, Cosmic-ray physics with icecube, Advances in Space Research 51 (2) (2013) 242 – 246, ¡ce:title¿The Origins of Cosmic Rays: Resolving Hess's Century-Old Puzzle¡/ce:title¿. doi:http://dx.doi.org/10.1016/j.asr.2011.06.028. URL http://www.sciencedirect.com/science/article/pii/S0273117711004650

[39] P. B. Price, K. Woschnagg, D. Chirkin, Age vs depth of glacial ice at south pole, Geophysical Research Letters 27 (14) (2000) 2129–2132. doi:10.1029/2000GL011351. URL http://dx.doi.org/10.1029/2000GL011351

[40] M. Ackermann, et al., South pole glacial climate reconstruction from multi-borehole laser particulate stratigraphy, Journal of Glaciology 59 (218) (2013) 1117–1128. doi:10.3189/2013JoG13J068. URL http://dx.doi.org/10.3189/2013JoG13J068

[41] P. Gabrielli, et al., Trace elements in Vostok Antarctic ice during the last four climatic cycles, Earth and Planetary Science Letters 234 (2005) 249. doi:10.1016/j.epsl.2005.03.001.

[42] W. I. Rose, T. J. Bornhorst, , American Association of Petroleum Geologists (AAPG) Special Volumes SG 13 (1981) 13.

[43] M. Ackermann, et al., Optical properties of deep glacial ice at the south pole, Journal of Geophysical Research: Atmospheres 111 (D13) (2006) n/a–n/a. doi:10.1029/2005JD006687. URL http://dx.doi.org/10.1029/2005JD006687

[44] D. Engelkemeir, Nonlinear response of nai(tl) to photons, Review of Scientific Instruments 27 (8) (1956) 589–591. doi:10.1063/1.1715643.

[45] T. Jones, The nonproportional response of a nai(tl) crystal to diffracted x rays, Nuclear Instruments and Methods 15 (1) (1962) 55 – 58. doi:10.1016/0029-554X(62)90026-5.

[46] A. Collinson, R. Hill, The fluorescent response of nai(tl) and csi(tl) to x rays and rays, Proceedings of the Physical Society 81 (5) (1963) 883. doi:10.1088/0370-1328/81/5/313.

[47] I. Khodyuk, P. Rodnyi, P. Dorenbos, Non-proportional scintillation response of NaI:Tl to low energy X-ray photons and electrons, J.Appl.Phys. 107 (2010) 113513. arXiv:1102.3799, doi:10.1063/1.3431009.

[48] J. Back, Y. Ramachers, ACTIVIA: Calculation of Isotope Production Cross-sections and Yields, Nucl.Instrum.Meth. A586 (2008) 286–294. arXiv:0709.3472, doi:10.1016/j.nima.2007.12.008.

[49] M. Laubenstein, G. Heusser, Cosmogenic radionuclides in metals as indicator for sea level exposure history, Applied Radiation and Isotopes 67 (2009) 750.

[50] B. N. L. National Nuclear Data Center, Nudat (nuclear structure and decay data) (March 18 2008).

[51] R. Bernabei, et al., The DAMA/LIBRA apparatus, Nucl.Instrum.Meth. A592 (2008) 297–315. arXiv:0804.2738, doi:10.1016/j.nima.2008.04.082.

[52] E. Sakai, Recent Measurements on Scintillator-Photodetector Systems, IEEE Transactions on Nuclear Science 34 (1987) 418–422. doi:10.1109/TNS.1987.4337375.

[53] Ilias database on radiopurity of materials. URL http://radiopurity.in2p3.fr

[54] S. Agostinelli, et al., GEANT4: A Simulation toolkit, Nucl.Instrum.Meth. A506 (2003) 250–303. doi:10.1016/S0168-9002(03)01368-8.

[55] J. Allison, et al., Geant4 developments and applications, IEEE Trans.Nucl.Sci. 53 (2006) 270. doi:10.1109/TNS.2006.869826.

[56] S. G. Crystals, Nai(tl) and polyscin nai(tl) sodium iodide scintillation material (7 2008).
URL http://www.detectors.saint-gobain.com